Design of compositionally modulated materials for controlled strain release during deformation through phase-field simulations

Dong Wang, Jiaming Zhu, Tianlong Zhang, and Yunzhi Wang*

Impurity segregation and solute partitioning, which can lead to microscale concentration modulations (microCMs), are common phenomena in materials processed through various methods. Traditionally, these microCMs have been viewed as undesirable, necessitating costly homogenization treatments for their removal. However, in this study, we introduce an innovative alloy design strategy that capitalizes on the potential benefits offered by microCMs, as revealed through phase-field simulations. The majority of our simulation predictions have received strong support from experimental investigations, and these predictions have guided the development of new experimental designs for microCM alloys with exceptional properties. We highlight two notable examples. The first example demonstrates how microCMs can be strategically employed to regulate martensitic transformations, transforming them from typical sharp first-order transitions into broadly smeared continuous transitions. This modification results in quasi-linear superelasticity with an exceptionally low apparent Young's modulus, as well as Invar and Elinvar anomalies. The second example showcases how microCMs can be harnessed to activate various solid-state phase-transformation mechanisms in distinct locations, including congruent transformation, pseudospinodal decomposition, and nucleation-and-growth, leading to microstructurally modulated materials with excellent comprehensive mechanical properties. These studies challenge the conventional view of microCMs as unwanted byproducts, demonstrating their potential as a valuable resource for designing alloys with outstanding characteristics.

Introduction

Materials prepared through diverse processing methods inherently exhibit both compositional and structural heterogeneity at nano- and micrometer scales.[1,2] Achieving precise control over the microstructures of materials, and consequently their properties, necessitates the inclusion of homogenization treatment as a pivotal step in materials processing. Nevertheless, materials with homogeneous microstructures have encountered significant challenges in achieving a substantially improved combination of properties, facing tradeoffs between strength and ductility[3,4] as well as between yield strength and elastic modulus.[5,6] To mitigate these tradeoffs, various strategies have been employed, such as introducing heterogeneous microstructures such as gradient or harmonic grain structures,[7] hierarchical precipitate microstructures,[8,9] and nanoscale martensitic domain structures.[6,10]

Looking into the nature of shear deformation of materials, whether it is carried by dislocations, mechanical twinning, or martensitic transformations in crystalline solids, and shear transformation zones (STZs) in amorphous solids, we recognize some key common features, including autocatalysis driven by long-range elastic interactions and the occurrence of strain avalanches after yielding. Thus, we hypothesize that if we could mitigate the autocatalysis by appropriate

Dong Wang, Frontier Institute of Science and Technology, State Key Laboratory for Mechanical Behavior of Materials, Xi'an Jiaotong University, Xi'an, China; wang_dong1223@xjtu.edu.cn
Jiaming Zhu, School of Civil Engineering, Shandong University, Jinan, China; Institute of Materials Intelligent Technology, Liaoning Academy of Materials, Shenyang, China; Shenzhen Research Institute of Shandong University, Shenzhen, Guangdong Province, China; zhujiaming@sdu.edu.cn
Tianlong Zhang, Department of Mechanical and Aerospace Engineering, The Hong Kong University of Science and Technology, Hong Kong, China; tianlong@ust.hk
Yunzhi Wang, Department of Materials Science and Engineering, The Ohio State University, Columbus, USA; wang.363@osu.edu
*Corresponding author
doi:10.1557/s43577-024-00721-w

microstructure engineering, we could achieve desired stress–strain behaviors for specific applications.

Phase stability and phase-transformation mechanisms are sensitive functions of alloy composition and, thus, they will modulate in a compositionally modulated material. This offers us the opportunity for engineer specific microstructures to effectively suppress autocatalysis and allow for a controlled strain release during either pseudoelastic[11,12] or plastic deformations[13,14] by controlling the wavelength, amplitude, and mean of the composition modulations at nano- and micrometer scales (dubbed microCM hereafter). Previous studies have shown that concentration inhomogeneities in crystalline solids often give rise to inhomogeneities in lattice parameter, elastic modulus, and phase stability that can have profound influences on microstructural development in microCM alloys and, hence, on their diverse properties.[15] Therefore, microCMs hold significant promises. Nevertheless, exploring the design variables of concentration modulations, including amplitude, wavelength, and mean, by experiment alone can be both costly and time-consuming.

The phase-field method is uniquely positioned to describe compositional and structural heterogeneities and their effects on phase transformations using continuous field variables (i.e., order parameters) to characterize the microstructure, allowing one to capture effectively the complex interplay between local chemical composition and structural transformations.[16–19] In this article, we demonstrate that high-throughput phase-field simulations could significantly accelerate the design and optimization of microCM alloys for functional and structural applications. In the first example, we will showcase how to utilize microCMs to regulate martensitic transformations (MTs) in shape-memory alloys (SMAs) by suppressing autocatalysis and turn the transformations from typical sharp first-order transitions with strain avalanches into continuous transformations with quasi-linear superelasticity and exceptionally low apparent Young's modulus. The simulation predictions seem to be supported by experimental findings in the literature. In the second example, we demonstrate how microCMs could be harnessed to activate distinct solid-state phase-transformation mechanisms in different locations of a microCM alloy, leading to microstructurally modulated materials with exceptional comprehensive mechanical properties.

Design and optimization of microCM ferroelastic materials

Reducing the modulus of metallic orthopedic implants (such as Ti alloys) to match that of natural bones (~20 GPa) is critical for avoiding the longstanding "stress shielding" problem in bone implant applications,[20–22] but it imposes a great challenge to physical metallurgy principles.[5,23,24] The typical yield strength of Ti alloys is on the order of 1 GPa. If the alloy is required to have a 20 GPa modulus, then it must have an elastic strain limit of 5% to retain its yield strength of 1 GPa. That would be an order of magnitude larger than the elastic strain limit observed in most metals (<0.5%). Thus, one must rely on alternative recoverable strain carriers, free from the limits of true elasticity, such as the pseudoelasticity related to reversible, stress-induced structural phase transformations such as MTs in SMAs.[25–27] However, the highly nonlinear pseudoelasticity associated with normal MTs with high Young's modulus and strain avalanche (**Figure 1**a) makes the conventional SMAs unsuitable for such applications.

One of the strategies to solve this critical problem is by developing appropriate microCMs to suppress autocatalysis and converting the highly nonlinear pseudoelastic deformation (Figure 1a) into a linear superelastic deformation (Figure 1b) with controlled strain release during MTs. We hypothesize that by microCM design (see schematics in Figure 1d) one can induce appropriate spatial variations in the starting temperature (M_s) and critical stress (σ_{Ms}) for thermally induced and stress-induced MTs, respectively. The spatial variations in M_s and σ_{Ms} will create nano-confinements to the MT process, effectively suppress autocatalysis and fundamentally change the MT characteristics from abrupt to gradual, which will lead to microCM ferroelastic materials that are superstrong, linear superelastic, avalanche- and hysteresis-free, and have ultralow modulus. This hypothesis is based on the fact that both M_s and σ_{Ms} are strong functions of alloy composition (see Figure 1c). To test this hypothesis, we have carried out extensive phase-field simulation studies[6,28–34] and these studies indeed demonstrate controlled strain release and exceptional properties not found in the compositionally homogeneous counterparts, including linear superelasticity, ultralow elastic modulus, and Invar and Elinvar anomalies in microCM SMAs and multifunctional metastable β-Ti alloys.[6,28–30,32,33,35–40] Detailed examples are presented next.

Design of microCM metastable β-Ti alloys

As a representative group among multifunctional metastable β-Ti alloys, Ti–Nb-based alloys have emerged as highly promising candidates for advanced biomedical applications. This appeal is attributed to their exceptional biocompatibility and distinctive physical and mechanical attributes, including superelasticity across a broad temperature range, low modulus, high strength, good ductility, and the ability to fine-tune their coefficients of thermal expansion. Notably, the presence of nanoscale concentration modulations with Nb-lean and Nb-rich regions has been identified through 3D atom probe tomography (APT).[39] However, how the roles played by the microCMs in achieving their outstanding physical and mechanical properties are unclear.

To understand the unique stress–strain response of this alloy system, high-throughput phase-field simulations have been carried out to study stress-induced MT in a microCM Ti–Nb-based alloy, Ti2448 (short for Ti–24Nb–4Zr–8Sn–0.1O in wt%), with variable wavelength and amplitudes. A miscibility gap has been reported for Ti–Nb binary system[35] and CALPHAD calculations[41] using a Thermo-Calc TCTi3 database

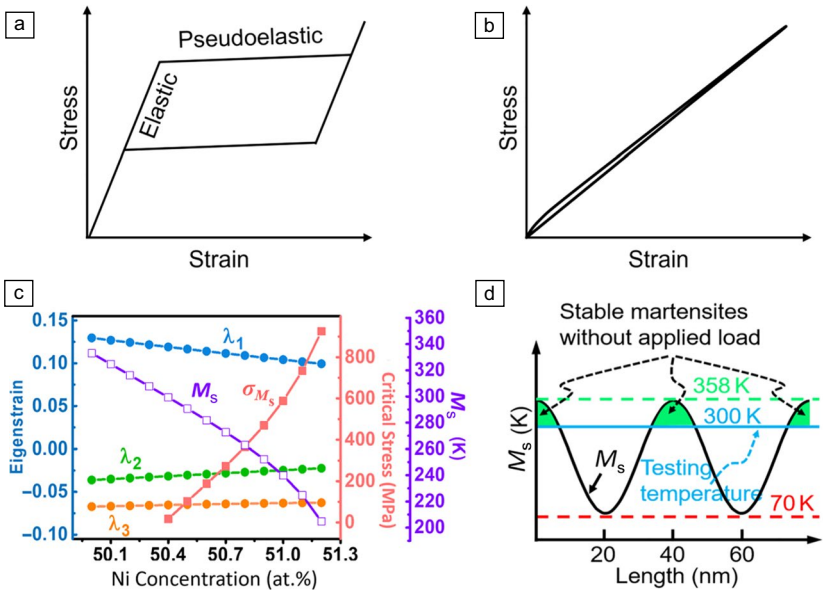

Figure 1. Schematic drawings of typical stress–strain curves anticipated for (a) highly nonlinear pseudoelastic deformation carried by unconstrained martensitic transformation (MT) in NiTi shape-memory alloy (SMA) having a uniform Ni concentration and (b) linear superelastic deformation with ultralow Young's modulus carried out by confined MT in NiTi SMA having nanoscale concentration modulations. (c) Dependence of martensitic transformation start temperature (M_s), critical stress (σ_{Ms}), and eigenstrains (λ_1–λ_3) on Ni concentration in NiTi SMA. (d) Schematic drawing of the M_s modulation corresponding to Ni concentration modulation. Regions with M_s above the testing temperature are highlighted in green, where martensite is stable.[6,28] (a, b, d) Adapted with permission from Reference 6. (CC BY 4.0). (c) Adapted with permission from Reference 28. © 2020 Elsevier.

also show spinodal decomposition in Ti2448, with microCMs of Nb, Ti, and Sn within a temperature range of 750–900°C, above the β-transus. MicroCMs in the parent β phase of Ti2448 have also been reported in recent experimental studies.[35] Spinodal decompositions typically produce microCMs at nanometer scales in three dimensions (3D) with interpenetrating morphologies (see **Figure 2**a). Such microstructures are incompatible with the self-accommodating polytwinned α″ martensitic domain structures[42] and, thus, would impose confinements to the MT and alter its characteristics. However, the effectiveness and strength of the confinements will depend on the wavelength, amplitude, and mean of such microCMs. For example, the nucleation of martensite will be delayed to significantly higher stress levels (or lower temperatures) when the wavelength is too small and amplitude is too high (for a given mean) to accommodate the self-accommodating martensitic nuclei. On the other hand, if the wavelength of the microCM is too large relative to the self-accommodating martensitic domain size or the amplitude is too small, the confinement will be too weak to suppress completely the autocatalysis and strain avalanche.

Our high-throughput phase-field simulations have revealed how the wavelength and amplitude of microCMs, generated through spinodal decomposition, impact the MT in Ti2448.[6,29]

The dependence of M_s and the transformation strain on Nb concentration in Ti2448 are available from the literature[43,44] and is shown in Figure 2g. Figure 2a shows the simulation results of a microCM of Nb in a single crystal (with an average Nb concentration of 15 at.%) produced by spinodal decomposition in the parent phase. The one-dimensional (1D) concentration wave along the body-diagonal of the computational cell and the statistical distribution of voxels with different Nb concentrations in the computational cell as a function of aging time for the spinodal decomposition are shown in Figure 2b–c, respectively. Being concentration-dependent, σ_{Ms} and the transformation strain modulate in space accompanying the microCM in the system. This leads to drastically different stress–strain (SS) curves (in terms of the hysteresis and critical stress for the MT, and a transition from pseudoelastic to superelastic behavior) for systems having different microCMs (in terms of wavelength and amplitude), as shown in Figure 2d. These differences are striking, ranging from substantial stress hysteresis and an evident stress plateau (indicative of strong nonlinear pseudoelasticity) to more slender curves (close to linear superelastic) with minimal hysteresis. Correspondingly, the volume fraction of martensite versus applied stress curves showcase a similar transition, marking the shift from a sharp first-order MT to a higher-order, continuous transition (Figure 2e). Figure 2f shows the lattice correspondence between β phase and α phase.

An example of the detailed microstructural evolution during the stress-induced MT upon loading and unloading is shown in **Figure 3**. In contrast to a compositionally uniform system, the stability of martensite and thus M_s modulate following the microCM. Upon loading, martensitic particles of preferred variants first appear in the Nb-leanest regions where the M_s is the highest (see Figure 2g) and σ_{Ms} is the lowest. Because the surrounding layers require higher σ_{Ms} to transform, the MT can only proceed by a limited amount until the stress level reaches the σ_{Ms} of the adjacent layer. This effectively shut off the self-autocatalysis and avoided strain avalanche, and the MT proceeded gradually toward Nb-richer and richer regions with increasing external load (Figure 3a–c, k). At the end of loading, most of the computational cell is occupied by martensite, but retained austenite stays in regions of the lowest M_s and highest σ_{Ms} (see the red oval in Figure 3d).

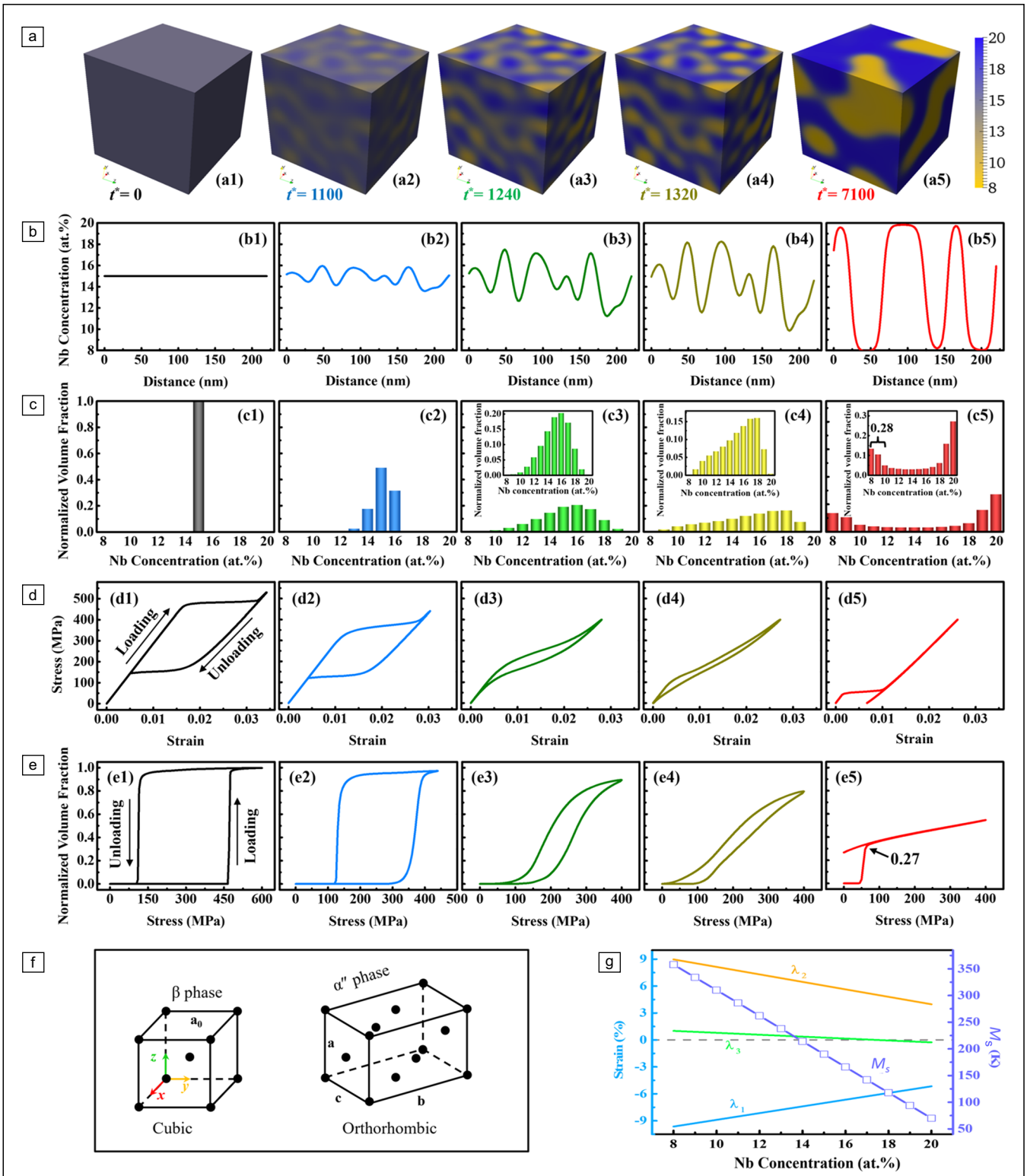

Figure 2. (a) Nb concentration modulation resulting from spinodal decomposition at different aging times. (b) One-dimensional Nb concentration profiles. (c) Statistical distributions of voxels with specific Nb concentrations in the computational cell. (d) Stress–strain curves during uniaxial tension along [100]. (e) The normalized volume fraction of martensite during cyclic loading. (f) Lattice correspondence between β (parent) and α″ (martensite) phases. (g) Dependence of martensitic transformation temperature (M_s) and eigenstrains (λ_1–λ_3) on Nb concentration in TiNb shape-memory alloy.[29] t^* is the dimensionless time step in our simulations. Adapted with permission from Reference 29. © 2017 Elsevier.

During unloading, the reverse transformation starts from these retained austenite regions, circumventing the need for nucleation of the austenite phase, and proceeds following a reverse sequence of the loading process (Figure 3e–h, l). Figure 3i shows the related stress–strain curve and Figure 3j concentration isosurface with Nb concentration of 9.3% and 19 percent.

Thus, these phase-field simulations have demonstrated that the overall MT characteristics can be effectively tuned from a typically first-order transition to a high order such as continuous transition by appropriate microCMs produced by spinodal decomposition through controlling the decomposition time (Figure 2a). These simulation predictions seem to be supported by recent experimental observations.[35,45] The simulation results reveal quantitative details on how the wavelength and amplitude of the microCMs vary with the progression of spinodal decomposition, and how microCMs influence the stress–strain behavior (such as the apparent Young's modulus and the shapes and hysteresis of the stress–strain [SS] curves as shown in Figure 2d) in Ti2448. Thus, these simulations could provide useful guidance for the design of microCM ferroelastic alloys for desired stress–strain behaviors.

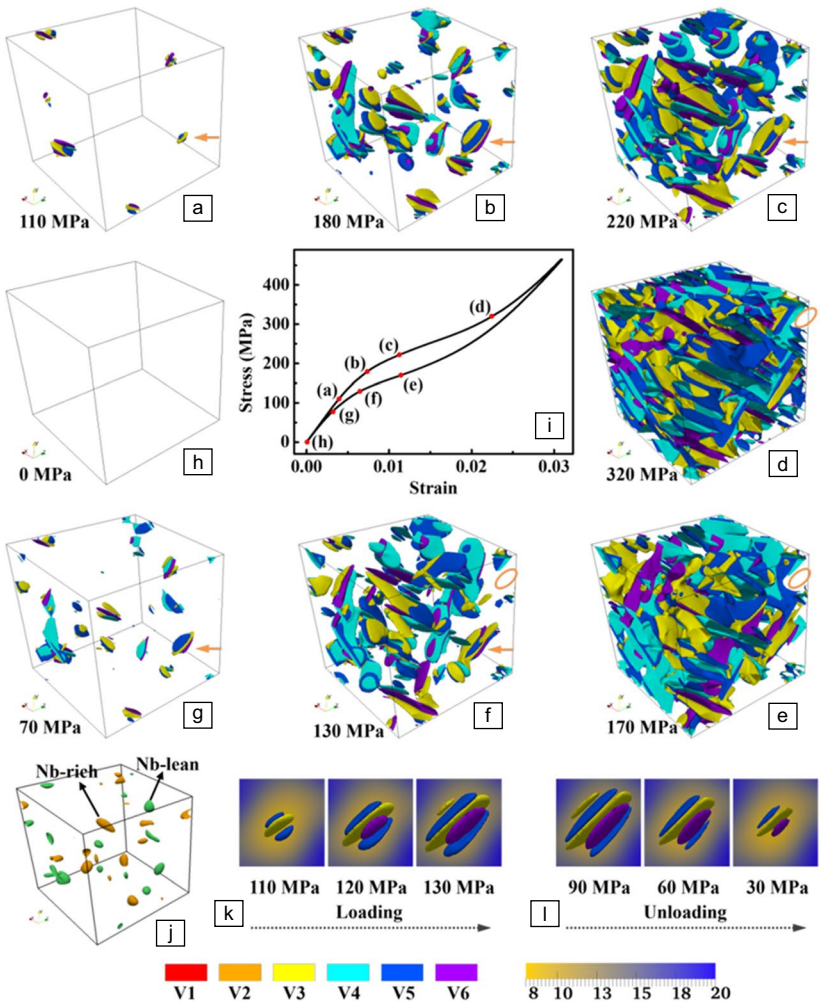

Figure 3. Microstructure evolution during martensitic transformation in a concentration modulated system during loading [(a–d), along $[100]_\beta$], and unloading (e–h) processes. The locations of the microstructural states in (a–h) on the stress–strain curve are indicated by the red dots in (i). In (a–h), the parent phase is set to be transparent and different variants (V) of the martensite are plotted as isosurfaces with different colors, as indicated in the color map at the bottom. (j) Nb-lean (green) and Nb-rich (orange) regions in the parent phase, where the green and orange isosurfaces correspond to Nb concentration of 9.3 and 19.0 at.%, respectively. (k) and (l) are close-up observations of the growth and shrinkage of the martensitic particle indicated by the arrows during loading and unloading, respectively. The background in (k) and (l) shows the Nb concentration distribution in the parent phase around the martensitic particle.[29] Adapted with permission from Reference 29. © 2017 Elsevier.

Furthermore, we have also demonstrated by phase-field simulations how to achieve simultaneously ultralow apparent Young's modulus (12 GPa), nearly zero hysteresis, and linear superelasticity with a large elastic strain limit of 2.7% by taking advantage of a synergic effect between microCM and prestraining (i.e., by adjusting the microCM to introduce preexisting martensitic nuclei via prestraining to circumvent the nucleation events during the MT). As one may already note, the SS curves obtained in Figure 2d exhibit noticeable hysteresis and have an apparent Young's modulus (for a single crystal) that is limited to 29.3 GPa. To achieve an ultralow apparent Young's modulus, nearly zero hysteresis, and linear superelasticity with a substantial elastic strain limit, a prestraining has been implemented in our phase-field simulations, as shown in **Figure 4**. Figure 4a(i) shows the Nb concentration in the spinodally decomposed Ti2448. The Nb-lean and Nb-rich regions form a typical interpenetrating domain network. Owing to the microCM in the parent phase, the hysteresis associated with the stress-induced MT is reduced drastically, as shown in Figure 2d, indicating that the mechanical behavior of the alloy depends strongly on the microCM. The SS curve in Figure 4a(ii), after the stress plateau, becomes almost linear and hysteresis-free. This finding implies that an almost linear pseudoelasticity in the entire stress or strain range could be achieved if the initial hysteresis could be eliminated. We demonstrate next that this can be achieved by adjusting the amplitude of the

microCM + prestraining. Figure 4b(i) shows the existence of abundant retained martensitic particles after the unloading of the first loading cycle in the microCM modulated systems. This is because the martensitic phase is more stable in the Nb-lean regions for the chosen microCM amplitude at the testing temperature. If we use the first loading–unloading cycle as prestraining (or training), then the retained martensitic particles will serve as operational nuclei and are ready to grow in subsequent loadings and, hence, eliminate the initial strain plateau and hysteresis associated with the need of nucleating martensite. As demonstrated in Figure 4b(ii), the SS curve obtained during the second loading–unloading cycle is almost hysteresis-free and almost linear, exhibiting a superelastic strain of ~2.7% at 400 MPa, with an apparent Young's modulus of 12 GPa.

Combined density functional theory (DFT) calculations and phase-field simulations also revealed a new strategy in designing Ti–Nb-based alloys with exceptional mechanical properties (linear superelastic, hysteresis-free, and ultralow modulus). In addition to the conventional martensitic phase α″ (shear + shuffle), shuffle-dominated O′ nanodomains were also observed in Ti–Nb-based alloys.[38] These shuffle-dominated O′ nanodomains can significantly influence the mechanical properties by affecting the formation of deformation twins and subsequent

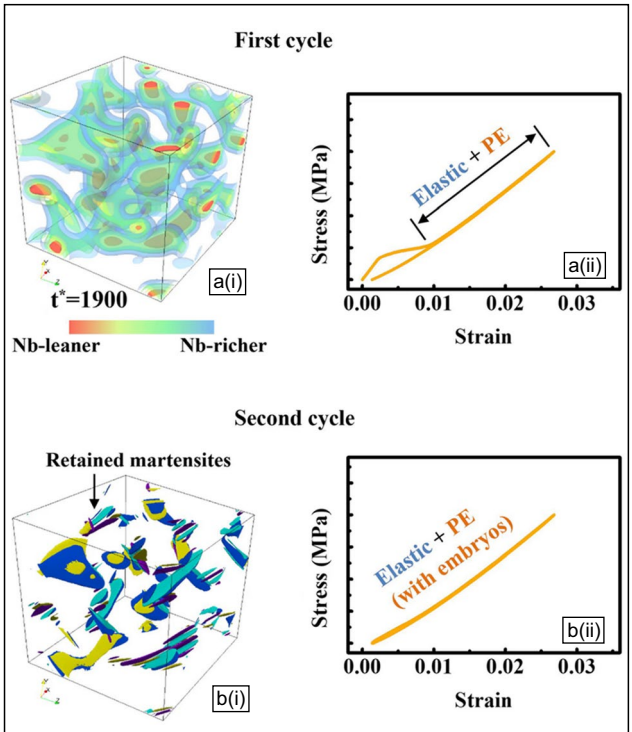

Figure 4. (a[i]) Modulated Nb concentrations. (a[ii]) First loading–unloading stress–strain curves under uniaxial tension along [001]. (b[i]) Microstructures following unloading after the first loading–unloading cycle as shown in (a[ii]). (b[ii]) Stress–strain curves for the second loading–unloading cycle.[6] PE, pseudoelastic. *t** is the dimensionless time step in simulations. Adapted with permission from Reference 6. (CC BY 4.0).

α″ martensite.[37] This is because the presence of the shuffle-dominated intermediate state of the O′ phase suggests that atomic shuffle precedes shear in the β → α″ transformation in Ti–Nb-based alloys and the O′ phase serves as the precursor of the α″ phase because they share the same shear modes. Crystallographic analysis[46,47] shows that if the shuffle takes place first, then the shear modes are severely limited.[31,38] So, it is the nano shuffle domains that set the tone for the β → α″ transformation (i.e., the nano shuffle domains lead to nano martensitic domains).[38] Note that there is no long-range elastic interaction among the shuffle domains because of the lack of shear and the shuffle domains are randomly distributed.

We hypothesize that if one could utilize the nanoscale CM to lock nano shuffle domains and then utilize the shuffle modes to lock the shear modes, then one would be able to suppress autocatalysis and turn the MT into a strain glass transition, the former yields long-range ordered, internally twinned martensitic plates (i.e., ordered strain patterns or strain crystals), while the latter yields randomly distributed nanodomains of martensite (i.e., disordered strain patterns or strain glass),[48–50] offering quasi-linear superelasticity with ultralow Young's modulus. To test this hypothesis, we first carry out first-principles calculations (**Figure 5**a–f) to reveal the dependence of the equilibrium values of the shuffle and shear components on Nb concentration, which consequently defines the different equilibrium structural states: α′ (characterized by complete shuffle and shear components), α″ (featuring partial shuffle and shear components), or O′ (dominated by the shuffle component). We then carry out phase-field simulations of the β → O′ → α″ transformations in microCM Ti–Nb-based alloys based on the first-principles calculations. The microstructure development is shown in Figure 5g–h. Because of the constraint of the nanoscale CM and the strong dependence of the shuffle mode on Nb concentration, the shuffle-dominated O′ domains do not grow and coarsen, which leads to nanodomains of α″ martensite during subsequent MT.

The progression of these microstructures during cooling is further examined through detailed views of local regions enclosed by the black dashed squares in Figure 5g, h. Initially, nanodomains of different variants of the O′ phase emerge, followed by the formation of nanodomains of α″ within the O′ domains. This pattern represents the characteristic microstructural feature of strain glasses. The O′ nanodomains materialize within the Nb-lean regions and grow toward the Nb-rich regions as the cooling progresses. Concurrently, the α″ nanodomains form at the centers of the O′ nanodomains and expand toward the edges. In Figure 5i, linear stress–strain curves with minimal hystereses and small residual strains are observed over a broad temperature range (5–400 K) in the phase-field simulations. Figure 5j exhibits the temperature dependence of the hysteresis and remain strain and Figure 5k shows the volume fraction change under loading at different temperatures. The calculated core–shell structures and hysteresis-free superelasticity are in good agreement with the experimental results.[35,38,39]

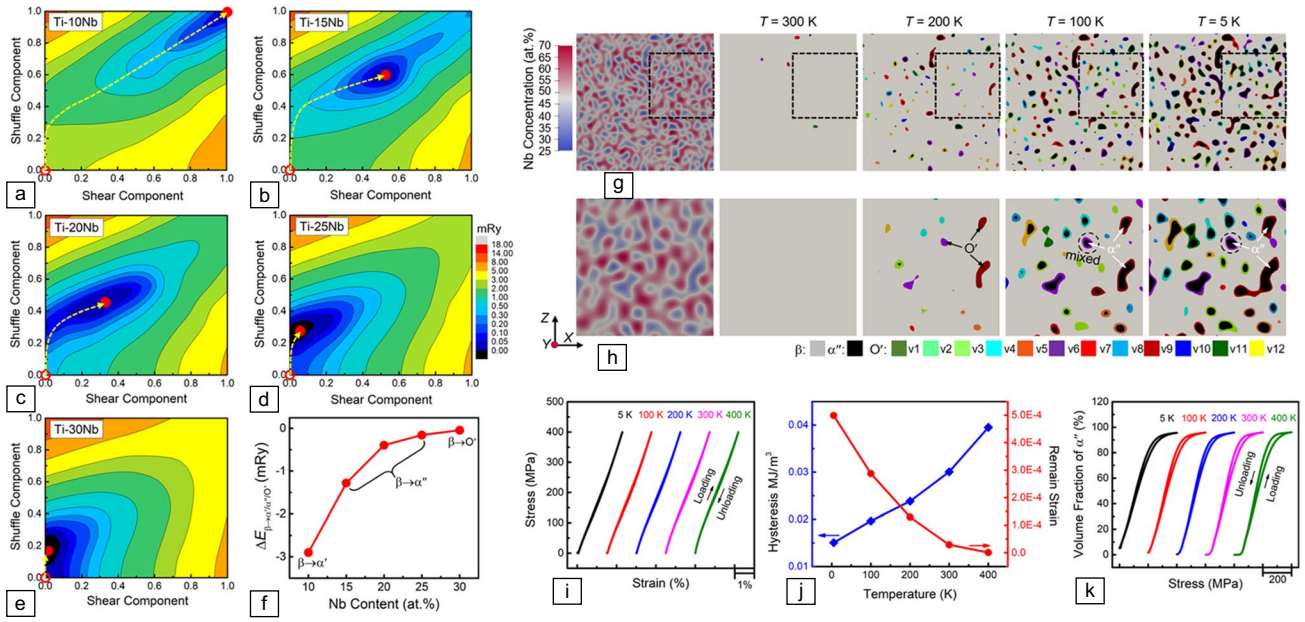

Figure 5. (a–e) Energy landscapes from density functional theory calculations depicting the β→α′, β→α″, and β→O′ transformations for Ti–xNb (at.%) as a function of the shear and shuffle components. The shuffle mode is (011)[0$\bar{1}$1]$_\beta$, and the shear mode is (2$\bar{1}$1)[11$\bar{1}$]$_\beta$. (f) Theoretical energy difference ($\Delta E_{\beta\to\alpha'}$, $\Delta E_{\beta\to\alpha''}$, and $\Delta E_{\beta\to O'}$, in mRy) with respect to Nb content. (g) A 2D Nb concentration field showing Nb concentration modulations and the related microstructural evolution of nanodomains during cooling. (h) A closer view of the area outlined by the dashed box in (g). (i) Stress–strain curves acquired from the first loading–unloading cycle. (j) Hysteresis area and residual strain derived from the stress–strain curves. (k) Volume fraction of stress-induced α″ martensite during the first cyclic loading.[31] Adapted with permission from Reference 31. © 2023 Elsevier.

Design of MicroCMs NiTi-based SMAs

Similar to the Ti–Nb-based metastable β-Ti alloys, the widely used NiTi-based SMAs also exhibit a strong composition-dependence of M_s and σ_{Ms} when the alloys are Ni-rich.[44,51] We hypothesize that if microCM NiTi SMAs with appropriate CMs (see **Figure 6**a–b) could be synthesized, linear superelasticity with vanishing hysteresis and ultralow Young's modulus could be achieved as well. To test this hypothesis, various compositionally graded NiTi (CG-NiTi) systems have been investigated by high-throughput phase-field simulations to identity the critical CMs that could convert the flag-shaped stress–strain (SS) curve to a linear one[28] (as shown schematically in Figure 1a–b). Since there is no miscibility gap in this alloy system, a multilayer configuration is considered, which could be synthesized by sputtering techniques. In Figure 6c–d, the microstructural evolution during the stress-induced MT and the corresponding SS curves of a multilayered bulk CG-NiTi during the first and second loading–unloading cycles are presented. These curves reveal that the multilayer CG-NiTi shown in Figure 6a–b, particularly in the second loading cycle, maintains linear superelasticity with a recoverable strain limit of 4.6% and an ultralow apparent Young's modulus of 8.7 GPa, accompanied by nearly zero hysteresis. As the external load increases, the martensitic domains formed in the bottom layer extend into the top layer, and the transformation front advances gradually. In other words, the interface between the austenite and martensite moves gradually from the Ni-lean layer toward the Ni-rich layer. Microstructure evolution observed during the second loading cycle suggests that martensite nucleation is avoided due to the retained martensite from the first loading–unloading cycle.

Figure 6e illustrates the effect of concentration gradient in the CG layer and the CG layer thickness on the stress–strain behavior of these multilayered CG-NiTi SMAs. All three CG systems considered exhibit mechanically stable linear superelasticity ranging from 4 to 4.9% (Figure 6f). However, a slightly larger hysteresis and lower apparent Young's modulus are observed as the concentration gradient becomes smaller, indicating a weaker regulation of the MT by the CG. In Figure 6g, the SS curves of the second cycle for systems with different thicknesses in the Ni-lean and Ni-rich layers are presented. These curves reveal that the CG-NiTi exhibits a reduced linear superelasticity as the Ni-lean and Ni-rich layers become thicker, as the former remains as martensite while the latter remains as austenite during the stress cycling and thus their reversible strain (elastic) is much smaller than that of the CG layer. It is noteworthy that the green curve in Figure 6g shows large hysteresis in contrast to the blue and yellow ones. This is because the prestraining effect disappears when the Ni-lean layer is too thin to stabilize the residual martensite, and nucleation of martensite is required upon each loading.

In addition to sputtering, precipitation[52] and dissolution[52,53] treatment could also produce nanoscale concentration modulation in Ni-rich NiTi SMAs. Phase-field

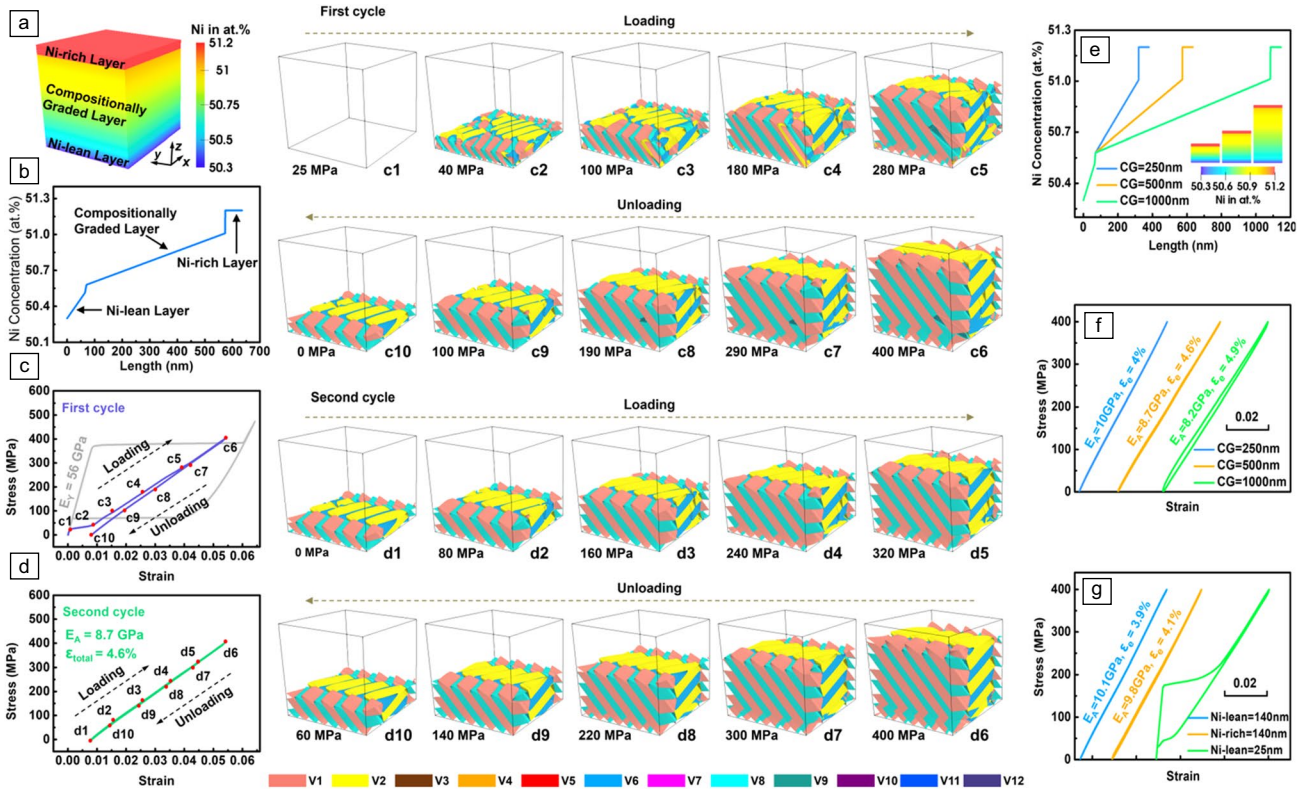

Figure 6. Phase-field simulation of stress–strain (SS) behavior and the corresponding microstructural evolution in a compositionally graded NiTi (compositionally graded [CG]-NiTi) alloy during loading–unloading cycles. (a) Concentration gradient in the designed CG-NiTi computational cell. (b) Variation of Ni concentration along the *z*-axis of the computation cell shown in (a). (c, d) Simulated SS curves of the system shown in (a) during first and second loading–unloading cycles, respectively. (c1-c0 and d1-d10) The microstructure evolution during the first and second loading–unloading cycles, respectively. (e) Concentration profiles of systems with three different thicknesses in the CG layer. The concentration gradients of the CG layers in these systems are 0.002, 0.001, and 0.0005 at.%/nm, respectively. The inset shows 2D views of the concentration distributions in these systems. (f) SS curves of the systems shown in (e). (g) SS curves of systems having thickness of 25 and 140 nm in the Ni-lean layer and 140 nm in the Ni-rich layer, respectively.[28] Adapted with permission from Reference 28. © 2020 Elsevier.

simulations have shown that Ni_4Ti_3 nanoprecipitates could be dissolved partially under up-quench + short-time solution treatment, generating microCMs. The microCMs also lead to a continuous MT behavior and superelasticity over a wide temperature range.

Design and optimization of microCM Ti alloys for structural applications

Titanium alloys have demonstrated an exceptional-specific strength among various structural materials, finding wide-ranging applications in various fields. Nevertheless, they still grapple with the inherent tradeoff between strength, work-hardening capacity, and ductility. Heterogeneous and gradient grain structures are believed to have the potential to overcome this dilemma via the so-called hetero-deformation mechanism.[54] However, achieving heterogeneous grain structure in Ti alloys is rather difficult and costly. We hypothesize that it is relatively easy to achieve an intragranular heterogeneous dual-phase precipitate microstructure and such a microstructure could lead to simultaneous enhancements in strength, work-hardenability, and ductility of Ti alloys. This hypothesis is based on the fact that a rich variety of phase-transformation pathways exist in Ti alloys and they are strongly composition-dependent. Thus, in a microCM Ti alloy, different transformation mechanisms will be activated in different locations having different local compositions (**Figure 7**). To test this hypothesis, phase-field simulations have been used to aid the design of microCM Ti alloys with modulated precipitate microstructures. It has greatly accelerated the screening of possible microCMs that could be synthesized through different experimental processes and by controlling different processing variables.

MicroCM Ti-alloy design by diffusion annealing of a multilayer system

The composition of Ti alloy significantly influences the precipitation process by altering the transformation pathways from congruent transformation to pseudo-spinodal decomposition to classical nucleation-and-growth.[55,56] As illustrated in Figure 7a, the alloy composition relative to the critical composition, C_0,

at which the free energy curves of the α and β phases intersect, determines the transformation pathways. When the alloy composition is located on the left of C_0 (in the red composition range in Figure 7a), a congruent β→α structural transformation takes place. Because of the relatively large precipitation driving force and the absence of solute partitioning (lack of long-range diffusion), this congruent structural transformation yields ultrafine α precipitates (Figure 7b). In cases where the alloy composition is located on the right of C_0, but close to C_0 (e.g., in the green composition range in Figure 7a), thermal fluctuations will make local compositions cross C_0, which, in turn, activates the congruent β→α structural transformation locally, followed by solute partitioning. This mechanism is referred to as pseudo-spinodal decomposition.[8,47,55,57,58] It leads to the formation of fine α precipitates (Figure 7c). When the alloy composition is located to the right of C_0 and significantly distant from it (e.g., in the blue composition range in Figure 7a), the β→α transformation adheres to the classical nucleation-and-growth mechanism, yielding a substantially coarser α precipitate microstructure (Figure 7d). This variation in precipitation mechanisms with alloy composition provides an opportunity to design a heterostructure featuring well-controlled precipitate microstructure gradients (Figure 7e) by introducing microCMs within the parent β phase.

Diffusion couple is one of the most intuitive approaches to achieve microCMs. As shown in Figure 7e, by placing two uniform Ti–V end-alloys together to form a diffusion couple in the unit cell of a multilayer system (under periodical boundary condition) in the phase-field simulation,[58] interdiffusion annealing at 650°C converts the initial square concentration wave into a sinusoidal one with V concentration varying continuously from 10.5 to 12.5 wt%. Then after a second step aging at lower temperatures (e.g., 550°C), the nucleation density and average size of the α precipitates change continuously in such a microCM Ti alloy because part of the system ($c > C_0$) undergoes conventional nucleation-and-growth, part of the system ($c \sim C_0$) undergoes pseudo-spinodal decomposition, and the other part of the system undergoes congruent structural transformation followed by decomposition. Such a modulated ultrafine to coarse precipitate microstructure is expected to have simultaneously enhanced strength and ductility.

MicroCM Ti-alloy design by spinodal decomposition

Miscibility gaps within the β phase have been documented in numerous Ti-X alloys, including Ti–Mo, Ti–V, Ti–Nb, Ti–Cr, Ti–Si, and Ti–Sc.[58] Notably, in contrast to the diffusion couple annealing approach, spinodal decomposition produces concentration modulations at much finer scales by continuous phase separation via uphill diffusion. This offers the opportunity to design well-controlled microCMs in the parent β phase and, correspondingly, well-controlled fine-scale precipitate microstructure modulations upon second annealing at lower temperatures below the β-transus.

Figure 8 showcases phase-field simulations of α precipitation by a precursory spinodal decomposition mechanism

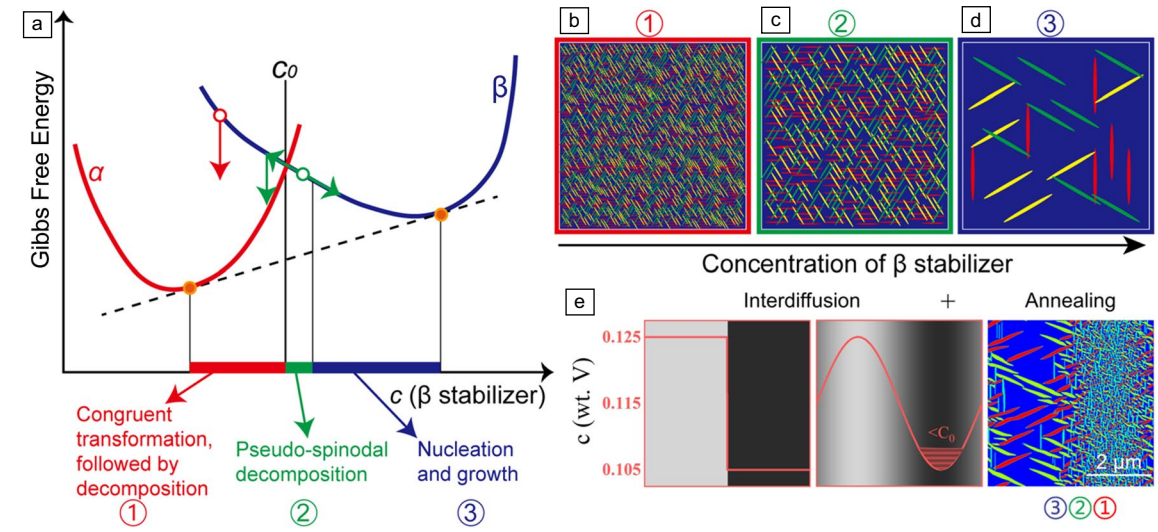

Figure 7. (a) Schematic diagram of the free energy curves of α and β phases as a function of β stabilizer concentration in Ti alloys. ① Composition range within which congruent β→α structural transformation occurs leading to an ultrafine α precipitate microstructure shown in (b). ② Composition range within which pseudo-spinodal decomposition mechanism operates, leading to a fine α precipitate microstructure shown in (c). ③ Composition range within which classical nucleation-and-growth mechanism operates, leading to a relatively coarse α precipitate microstructure shown in (d). (e) When a composition modulation is present in the β matrix by diffusion annealing of a diffusion couple, different precipitation mechanisms will operate simultaneously, resulting in a modulated precipitate microstructure.[58,59] (a–d) Adapted with permission from Reference 59. © 2023 Elsevier. (e) Adapted with permission from Reference 58. © 2020 Elsevier.

through a two-step annealing heat treatment.[58] At elevated temperatures above the β-transus, spinodal decomposition in the β phase takes place and generates a microstructure with isolated or interconnected solute-rich (β″, bright) and solute-lean (β′, black) domains, depending on the alloy composition and annealing time, as depicted in Figure 8a, c, and e. Subsequently, quenching to a lower temperature activates the congruent structural transformation followed by decomposition or the pseudo-spinodal decomposition mechanism within the solute-lean β′ regions. This two-step heat treatment leads to various novel heterogeneous precipitate microstructures with high density of α precipitates in the β′ regions alone, as evident in Figure 8b, d, f, and g, including an inverted bimodal microstructures (Figure 8d, g).

MicroCM Ti-alloy design by precipitate dissolution

MicroCMs in the β matrix of a Ti alloy could also be achieved by partial dissolution of α precipitates upon up-quench. In this case, the wavelength and amplitude can be controlled by the precipitation and up-quench heat treatments. To demonstrate this opportunity, a three-step heat treatment process is formulated in the phase-field simulations for a prototype binary Ti–Mo alloy. The simulation results are shown in **Figure 9**.[59] The three-step heat treatment consists of the following. Step 1: In this initial step, it is assumed that globular α_p precipitates (widely available in α+β Ti alloys) exist with an area fraction of approximately 20 percent. Step 2: The sample is up-quenched to the single β-phase region (at 920°C) and isothermally held for varying durations. During this period, the globular α_p precipitates undergo a complete structural transformation back to β. However, the homogenization of Mo concentration within the β matrix requires an extended time period. Initially, the "phantom" globular α_p precipitates are still visible (Figure 9b[ii]), but they gradually diminish with longer aging times (Figure 9c[ii], d[ii]). This results in alternating Mo-rich and Mo-lean regions within the β matrix, featuring different α-stabilizer-rich and α-stabilizer-lean compositions. Step 3: In this final step, samples are quenched to and aged at a lower temperature. This step leads to the formation of various α+β microstructures, including a bimodal microstructure composed of globular α_p and lamellar α, a heterostructure with alternating coarse and ultrafine lamellar α, structures with coarse and fine α plates, and a homogeneous structure with uniformly distributed α plates. The size scale of α plates in the homogeneous structure falls between that of the ultrafine and coarse α plates in the heterostructure. Additionally, as the aging temperature increases, both the coarse and ultrafine α plates undergo coarsening, although to different extents.

Encouraged and guided by these simulation results, a three-step heat treatment experiment has been carried out for Ti-55531 to develop heterogeneous precipitate microstructures. The results are shown in **Figure 10**. First, the as-received alloy was initially annealed at 800°C (within the α+β phase region) for 90 min to achieve a duplex microstructure with globular α_p precipitates, which are approximately 1–3 μm in diameter and account for about 20% of the area in the SEM image (Figure 10a). Subsequently, the globular α_p precipitates were partially dissolved by up-quenching the alloy to the single β-phase region and isothermally holding at 920°C for 3 min. The concentration distribution in Figure 10c has shown the existence of concentration modulation. Finally, the alloy was aged at 600°C for 120 min. This heterostructure formed exhibits an alternating

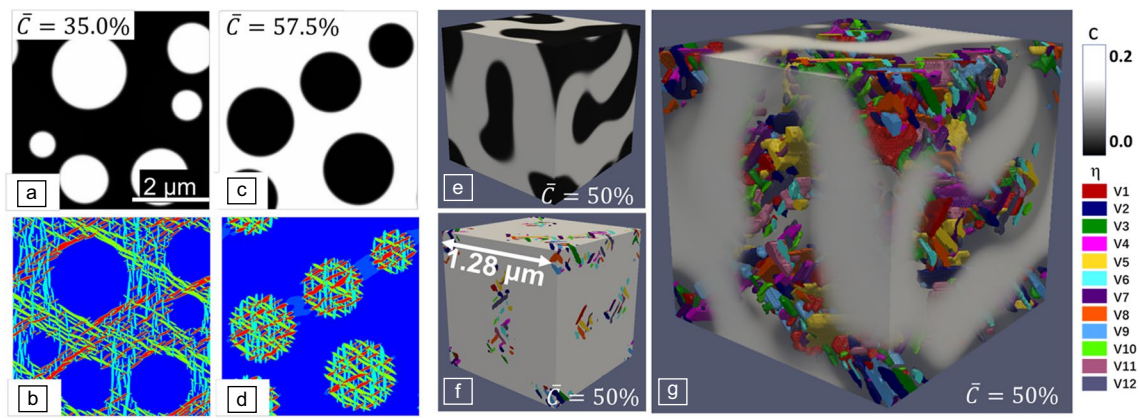

Figure 8. Microstructures for different alloy compositions obtained through the precursory spinodal decomposition mechanism. (a, b) $\bar{c}$ = 35 wt%; (c, d) $\bar{c}$ = 57.5 wt%; (e–g) $\bar{c}$ = 50 wt%. (a, c, e) The concentration field produced by spinodal decomposition in β, where the black regions are solute-lean β′ phase and the light gray regions are solute-rich β″ phase. (b, d, f) The structural order parameter field showing α precipitates formed in the solute-lean β′ regions. (g) Superposition of both the concentration (e) and structural order parameter (f) fields, showing a 3D interpenetrated α precipitate network structure.[58] Adapted with permission from Reference 58. © 2020 Elsevier.

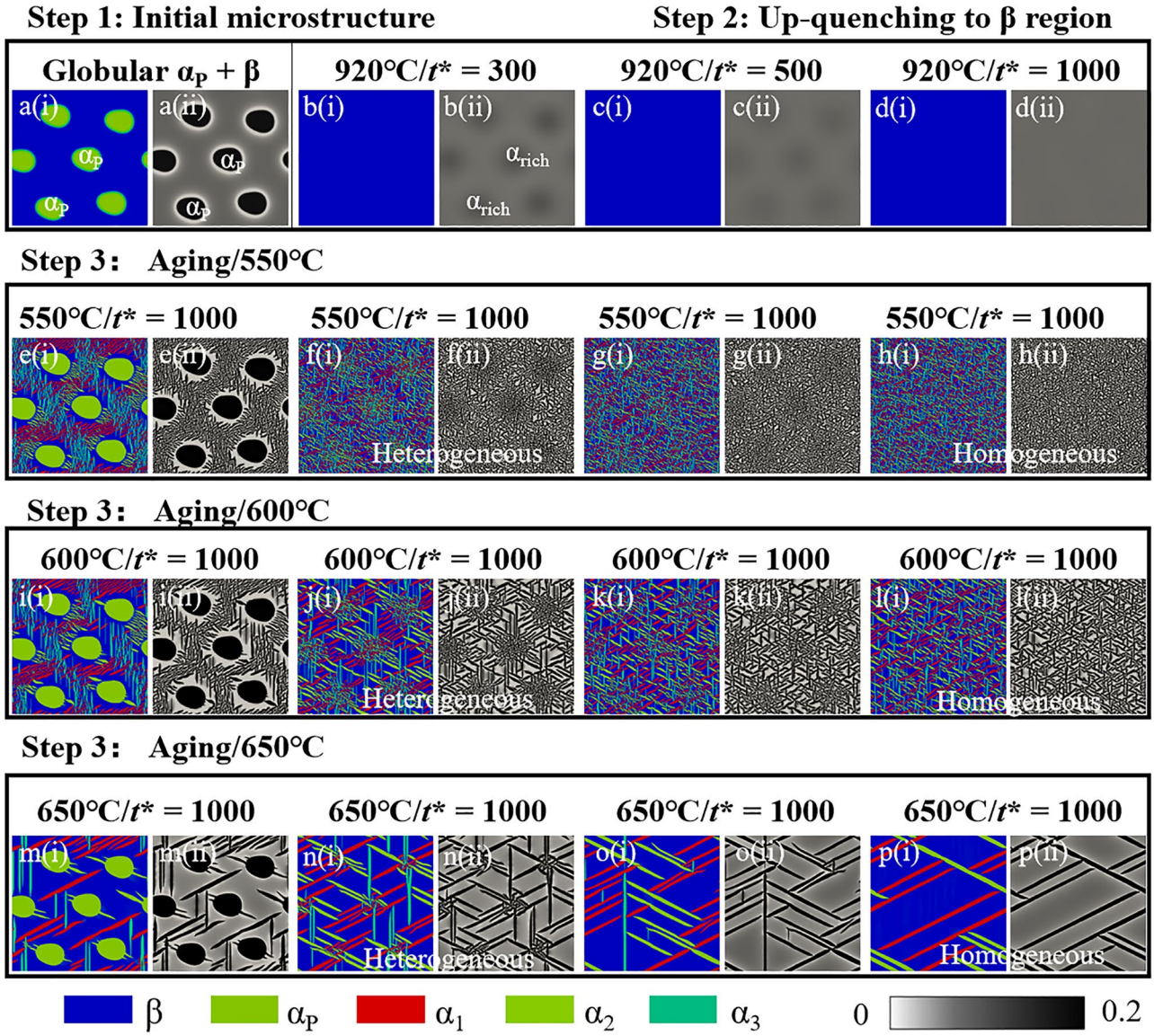

Figure 9. Simulated α precipitate microstructures produced by three-step heat treatment. (a[i], a[ii]) In Step 1 (structure and concentration, respectively) containing globular α_p embedded in β. In Step 2 (b[i]–d[ii]), the alloy is up-quenched to β-phase region (920°C) for different times. In Step 3 (e[i]–p[ii]), the systems are aged at 550, 600, and 650°C, respectively. The images in color represent the structural fields, where red, green, and blue represent the three variants of the α precipitates in 2D, and dark blue represents the β matrix. The images in grayscale represent the concentration field, where dark gray represents α precipitates and light gray represents the β matrix.[59] *t** is the dimensionless time step in simulations. Adapted with permission from Reference 59. © 2023 Elsevier.

coarse and ultrafine α precipitates (Figure 10d–f) and such a heterogeneous precipitate microstructure has been shown to exhibit significantly enhanced strength and ductility (Figure 10g–h). The ability to control the precipitate microstructures through this process showcases the potential for tailoring the mechanical properties of Ti alloy through relatively simple heat treatments. Such an approach can also be found in the manufacturing of microCM advanced high-strength dual-phase steels (AHSS)[60] by up-quench and partial dissolution of pearlite in an Mn eutectoid steel.

MicroCM Ti-alloy design by additive manufacturing

MicroCM Ti alloys can also be synthesized via 3D printing[61] and laser engineered net shaping (LENS),[62] as well as co-sputtering.[63] Inspired by the phase-field simulation results, experiments have been conducted to introduce microCMs via laser-powder bed fusion (L-PBF) using a mixture of two different types of alloy powders, Ti–6Al–4V (Ti64) and 316L.[64] **Figure 11** shows the typical microCM architecture achieved in an as-printed Ti64-(4.5 wt%)316L alloy.[64] It is readily seen the

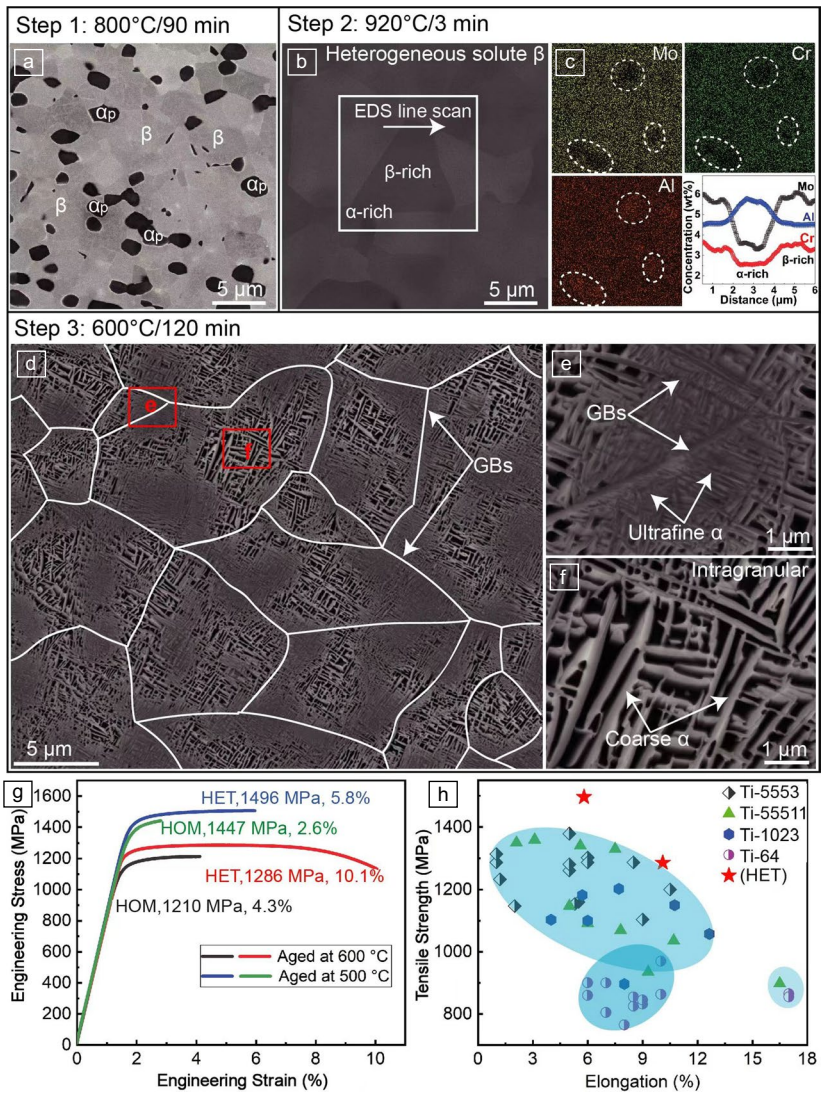

Figure 10. Heterostructure of Ti-55531 alloy obtained through three-step heat treatment: (a) Step 1, (b) Step 2, (c) concentration maps, (d) Step 3. (e, f) Fine and coarse α at different locations. (g) Comparison of tensile properties between Ti-55531 alloys having heterostructure and homogeneous structures. (h) Comparison of tensile properties of the heterostructured Ti-55531 (HET) with other Ti alloys.[59] EDS, energy-dispersive spectroscopy; GBs, grain boundaries. Adapted with permission from Reference 59. © 2023 Elsevier.

depletion of Ti, Al, and V (Ti64 elements) and the enrichment of Fe, Cr, and Ni (316L elements) in one of the swirls within the melt pool (Figure 11a), confirming the presence of microCMs. The TEM results provide a closer look at the concentration variations of different elements from β to α′ martensite (Figure 11b, c), which indicate that as the alloy continues to cool, the regions with lower 316L content undergo the β–α′ martensitic transformation, while the regions with higher 316L element content remain as the metastable β phase. Therefore, by modulating the β-phase stability via microCMs of the 316L elements, a highly dispersed dual-phase microstructure consisting of β and α′ phases has been achieved (see Figure 11e–i). This microstructure demonstrates a progressive transformation-induced plasticity (TRIP) effect, exhibiting an impressive tensile strength of approximately 1.3 GPa, a uniform elongation about 9%, and an outstanding work-hardening capacity exceeding 300 MPa.

Other means to produce microCM alloys

There are ample ways to create microCMs deliberately in materials processes, not limited to those we have demonstrated in the examples previously presented. For example, physical and chemical vapor deposition (PVD and CVD) and molecular-beam epitaxy (MBE) methods can be used to synthesize films with precisely controlled composition gradients.[65,66] Sol–gel techniques can create gels with varying concentrations in materials,[67] which can be subsequently processed to form microCMs in ceramics and composites. The choice of method depends on the specific materials and the desired microstructures.

Conclusions

In this article, we showcase how phase-field modeling has aided the design of microCM alloys with unique physical, functional, and mechanical properties. MicroCMs can be deliberately created in shape-memory alloys, titanium alloys, and advanced steels by employing methods such as spinodal decomposition, interdiffusion, partial dissolution of precipitates via up-quench, and incomplete mixing of two dissimilar alloy powders in the melt pool of L-PBF. The benefits of microCMs in these alloys include (a) taming the martensitic transformations from typical sharp first-order transitions into apparently continuous transitions and, thus, rendering the microCM SMAs and microCM metastable β-Ti-alloys quasi-linear superelastic with vanishing hysteresis, exceptionally low apparent Young's modulus, and Invar and Elinvar anomalies; (b) activating various solid-state phase-transformation mechanisms in distinct locations within microCM α + β Ti alloys, including congruent transformation, pseudo-spinodal decomposition, and nucleation-and-growth, which leads to the formation of microstructurally modulated

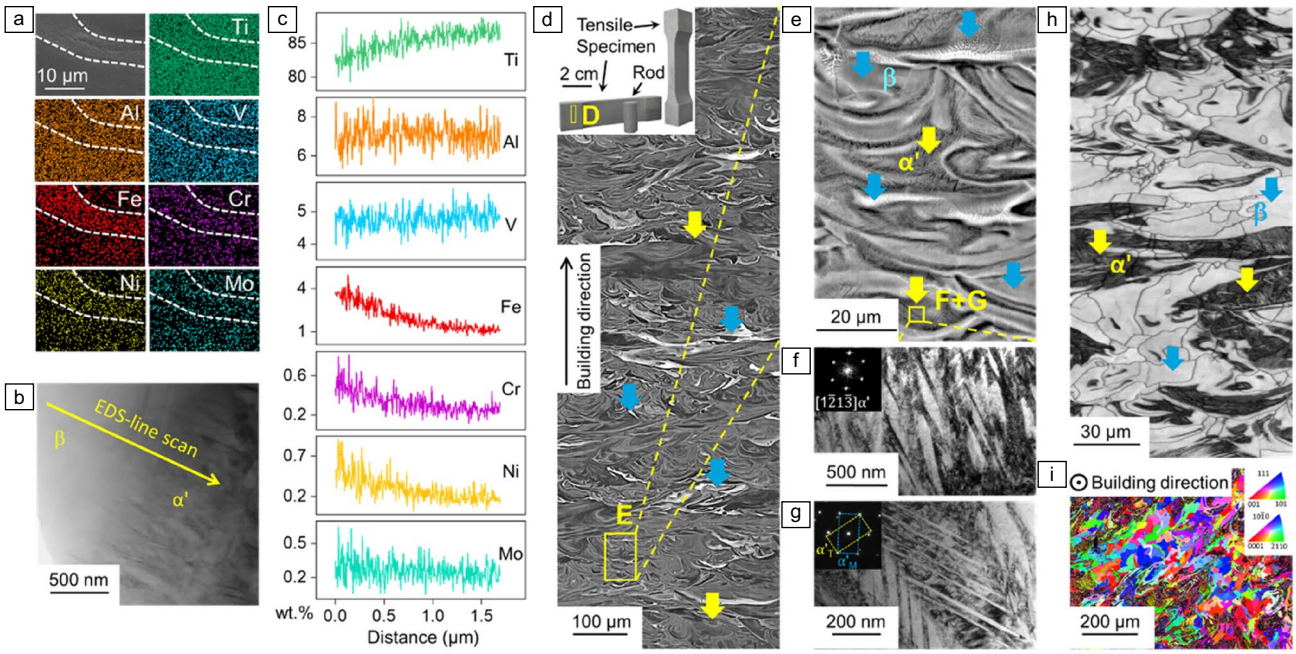

Figure 11. Microscale concentration modulations and microstructures of an as-printed Ti64-(4.5%)316L alloy. (a) Scanning electron microscopy-energy-dispersive spectroscopy (SEM–EDS) maps of different elements within one of the swirls of the melt pool. (b) Scanning transmission electron microscopy (TEM) image of the β–α′ interphase region. (c) Composition profiles along the EDS-line scan in (b). (d) Side-view cross-sectional backscattered electron (BSE) image. The inset shows a photograph of the as-printed Ti64-(4.5%)316L tensile specimen and rod. (e) Enlarged BSE image showing the lava-like heterogeneous microstructure. (f) Fine acicular α′ martensite as observed by TEM bright-field image. (g) Ultrafine twin structure as observed by TEM bright-field image. (h, i) Electron backscatter diffraction EBSD images of as-printed Ti64-(4.5%)316L. (h) Band contrast image of side-view cross section showing the ultrafine grain structure without columnar grains. (i) Inverse pole figure map of the top-view cross section showing grain orientations of β and α′ phases.[64] Adapted with permission from Reference 64. © 2021 AAAS.

Ti alloys with excellent comprehensive mechanical properties; and (c) modulated metastable/stable precipitate microstructures that offer synergistic combinations of dislocation plasticity and transformation-induced plasticity and, thus, high strength, work-hardenability, and uniform elongation. These findings highlight the significance of phase-field modeling in shaping a new alloy design strategy (i.e., microCM, to harness unprecedented properties).

Acknowledgments

Y.W. acknowledges the support from the National Science Foundation under Grant No. DMR-2333551. D.W. acknowledges the support from the National Natural Science Foundation of China (NSFC) (Grant Nos. 52171012 and 51931004), the National Key Research and Development Program of China (Grant No. 2021YFB3702603), and 111 project (BP2018008). J.Z. acknowledges the support from the National Natural Science Foundation of China (Grant No. 12372152), Qilu Young Talent Program of Shandong University, Zhejiang Lab Open Research Project (No. K2022PE0AB05), and Shandong Provincial Natural Science Foundation (ZR2023MA058) and Guangdong Basic and Applied Basic Research Foundation (No. 2023A1515011819 , 2024A1515012469). T.Z. acknowledges the support R9892 startup funding from The Hong Kong University of Science and Technology.

Author contributions

Y.W. designed this paper, and all authors contributed to the writing and revision of the manuscript.

Funding

Funding was provided by the National Science Foundation under Grant No. DMR-2333551 (Y.W.), the National Natural Science Foundation of China (Grant Nos. 52171012, 51931004, and 12372152) (D.W.), the National Natural Science Foundation of China (Grant No. 12372152), the support R9892 startup funding from The Hong Kong University of Science and Technology (T.L.Z.).

Data availability

Not applicable.

Conflict of interest

There is no conflict of interest.

References

1. M. Warmuzek, W. Ratuszek, G. Sek-Sas, *Mater. Charact.* **54**, 31 (2005)
2. G.S. Cole, *Metall. Trans.* **2**, 357 (1971)
3. K. Lu, *Science* **328**, 319 (2010)
4. E. Ma, T. Zhu, *Mater. Today* **20**, 323 (2017)
5. S. Ogata, J. Li, S. Yip, *Science* **298**, 807 (2002)
6. J.M. Zhu, Y.P. Gao, D. Wang, J. Li, T.Y. Zhang, Y.Z. Wang, *Mater. Horiz.* **6**(3), 515 (2019)
7. X.Y. Li, L. Lu, J.G. Li, X. Zhang, H.J. Gao, *Nat. Rev. Mater.* **5**, 706 (2020)
8. M.Y. Hao, P. Li, X.X. Li, T.L. Zhang, D. Wang, Q.Y. Sun, L.B. Liu, J.S. Li, Y.Y. Cui, R. Yang, D.S. Xu, *J. Mater. Sci. Technol.* **124**, 150 (2022)
9. Y.L. Wang, M.Y. Hao, D.A. Li, P. Li, Q.L. Liang, D. Wang, Y.F. Zheng, Q.Y. Sun, Y.Z. Wang, *Mater. Sci. Eng. A* **829**, 142117 (2022)
10. M.X. Fang, Y.C. Ji, Y. Ni, W.J. Wang, H.M. Zhang, X.F. Wang, A.D. Xiao, T.Y. Ma, S. Yang, X.B. Ren, *Phys. Rev. Lett.* **130**, 116102 (2023)
11. K. Otsuka, X.B. Ren, *Intermetallics* **7**, 511 (1999)
12. S.A. Shabalovskaya, *Bio-Med. Mater. Eng.* **6**, 267 (1996)
13. T. Saito, T. Furuta, J.H. Hwang, S. Kuramoto, K. Nishino, N. Suzuki, R. Chen, A. Yamada, K. Ito, Y. Seno, T. Nonaka, H. Ikehata, N. Nagasako, C. Iwamoto, Y. Ikuhara, T. Sakuma, *Science* **300**, 464 (2003)
14. Y.J. Zhou, Y. Zhang, Y.L. Wang, G.L. Chen, *Appl. Phys. Lett.* **90**, 181904 (2007)
15. E. Ma, J. Ding, *Mater. Today* **19**, 568 (2016)
16. I. Steinbach, *Model. Simul. Mater. Sci. Eng.* **17**, 073001 (2009)
17. Y.H. Zhao, H. Xing, L.J. Zhang, H.B. Huang, D.K. Sun, X.L. Dong, Y.X. Shen, J.C. Wang, *Acta Metall. Sin. (Engl. Lett.)* **36**, 1749 (2023)
18. Y.Z. Wang, J. Li, *Acta Mater.* **58**, 1212 (2010)
19. L.Q. Chen, *Annu. Rev. Mater. Res.* **32**, 113 (2002)
20. M. Geetha, A.K. Singh, R. Asokamani, A.K. Gogia, *Prog. Mater. Sci.* **54**, 397 (2009)
21. M. Long, H.J. Rack, *Biomaterials* **19**, 1621 (1998)
22. M. Niinomi, M. Nakai, *Int. J. Biomater.* **2011**, 836587 (2011)
23. J. Frenkel, *Z. Phys.* **37**, 572 (1926)
24. J. Li, *MRS Bull.* **32**(2), 151 (2007)
25. J.W. Christian, G.B. Olson, M. Cohen, *J. Phys. IV France* **05**, C8 (1995)
26. K. Ōtsuka, C.M. Wayman, *Shape Memory Materials* (Cambridge University Press, Cambridge, 1998)
27. E.K.H. Salje, *Annu. Rev. Mater. Res.* **42**(42), 265 (2012)
28. J.M. Zhu, D. Wang, Y.P. Gao, T.Y. Zhang, Y.Z. Wang, *Mater. Today* **33**, 17 (2020)
29. J.M. Zhu, Y.P. Gao, D. Wang, T.Y. Zhang, Y.Z. Wang, *Acta Mater.* **130**, 196 (2017)
30. J.M. Zhu, H.H. Wu, X.S. Yang, H. Huang, T.Y. Zhang, Y.Z. Wang, S.Q. Shi, *Acta Mater.* **181**, 99 (2019)
31. Y.T. Su, C.X. Liang, X. Sun, H.L. Zhang, Q.L. Liang, Y.F. Zheng, Y.L. Hao, R. Yang, D. Wang, D. Banerjee, Y.Z. Wang, *Acta Mater.* **246**, 118697 (2023)
32. D. Wang, S. Hou, Y. Wang, X.D. Ding, S. Ren, X.B. Ren, Y.Z. Wang, *Acta Mater.* **66**, 349 (2014)
33. D. Wang, Q.L. Liang, S.S. Zhao, P.Y. Zhao, T.L. Zhang, L.S. Cui, Y.Z. Wang, *Acta Mater.* **164**, 99 (2019)
34. L.X. Zhang, D. Wang, X.B. Ren, Y.Z. Wang, *Sci. Rep.* **5**, 11477 (2015)
35. Y.L. Hao, H.L. Wang, T. Li, J.M. Cairney, A.V. Ceguerra, Y.D. Wang, Y. Wang, D. Wang, E.G. Obbard, S.J. Li, R. Yang, *J. Mater. Sci. Technol.* **32**, 705 (2016)
36. Q. Liang, Y.F. Zheng, D. Wang, Y.L. Hao, R. Yang, Y.Z. Wang, H.L. Fraser, *Scr. Mater.* **158**, 95 (2019)
37. Q.L. Liang, Z. Kloenne, Y.F. Zheng, D. Wang, S. Antonov, Y.P. Gao, Y.L. Hao, R. Yang, Y.Z. Wang, H.L. Fraser, *Scr. Mater.* **177**, 181 (2020)
38. Q.L. Liang, D. Wang, Y.F. Zheng, S.S. Zhao, Y.P. Gao, Y.L. Hao, R. Yang, D. Banerjee, H.L. Fraser, Y.Z. Wang, *Acta Mater.* **186**, 415 (2020)
39. H.L. Wang, Y.L. Hao, S.Y. He, T. Li, J.M. Cairney, Y.D. Wang, Y. Wang, E.G. Obbard, F. Prima, K. Du, S. Li, R. Yang, *Acta Mater.* **135**, 330 (2017)
40. H.L. Wang, S.A.A. Shah, Y.L. Hao, F. Prima, T. Li, J.M. Cairney, Y.D. Wang, Y. Wang, E.G. Obbard, S.J. Li, R. Yang, *J. Alloys Compd.* **700**, 155 (2017)
41. K. Kadirvel, S.R. Koneru, Y.Z. Wang, *Scr. Mater.* **214**, 114657 (2022)
42. T. Inamura, J.I. Kim, H.Y. Kim, H. Hosoda, K. Wakashima, S. Miyazaki, *Philos. Mag.* **87**, 3325 (2007)
43. H.Y. Kim, J.I. Kim, T. Inamura, H. Hosoda, S. Miyazaki, *Mater. Sci. Eng. A* **438**, 839 (2006)
44. K. Otsuka, X. Ren, *Prog. Mater. Sci.* **50**, 511 (2005)
45. K. Tsuchiya, H. Sato, S. Edo, K. Marukawa, M. Umemoto, *Mater. Sci. Eng. A* **285**, 353 (2000)
46. D. Banerjee, J.C. Williams, *Acta Mater.* **61**, 844 (2013)
47. Y.F. Zheng, R.E.A. Williams, S.Y. Nag, R. Banerjee, H.L. Fraser, D. Banerjee, *Scr. Mater.* **116**, 49 (2016)
48. S. Sarkar, X.B. Ren, K. Otsuka, *Phys. Rev. Lett.* **95**, 205702 (2005)
49. D. Wang, Y.Z. Wang, Z. Zhang, X.B. Ren, *Phys. Rev. Lett.* **105**, 205702 (2010)
50. D. Wang, Y.C. Ji, X.B. Ren, Y.Z. Wang, *Annu. Rev. Mater. Res.* **52**, 159 (2022)
51. J. Frenzel, E.P. George, A. Dlouhy, C. Somsen, M.F.X. Wagner, G. Eggeler, *Acta Mater.* **58**, 3444 (2010)
52. D. Schryvers, W. Tirry, Z.Q. Yang, *Mater. Sci. Eng. A* **438**, 485 (2006)
53. T.J. Dong, T.F. Zhao, C.X. Liang, D. Wang, *Shape Mem. Superelast.* **9**, 321 (2023)
54. Y.T. Zhu, X.L. Wu, *Prog. Mater. Sci.* **131**, 101019 (2023)
55. A. Boyne, D. Wang, R.P. Shi, Y. Zheng, A. Behera, S. Nag, J.S. Tiley, H.L. Fraser, R. Banerjee, Y. Wang, *Acta Mater.* **64**, 188 (2014)
56. D. Wang, R.P. Shi, Y.F. Zheng, R. Banerjee, H.L. Fraser, Y.Z. Wang, *JOM* **66**(7), 1287 (2014)
57. Y. Ni, A.G. Khachaturyan, *Nat. Mater.* **8**, 410 (2009)
58. T.L. Zhang, D. Wang, Y.Z. Wang, *Acta Mater.* **196**, 409 (2020)
59. D. Wu, M.Y. Hao, T.L. Zhang, Z. Wang, J. Wang, G.H. Rao, L.G. Zhang, C.Y. Ding, K.C. Zhou, L.B. Liu, D. Wang, Y.Z. Wang, *Acta Mater.* **257**, 119182 (2023)
60. W.W. Sun, Y.X. Wu, S.C. Yang, C.R. Hutchinson, *Scr. Mater.* **146**, 60 (2018)
61. T.R. Jackson, H. Liu, N.M. Patrikalakis, E.M. Sachs, M.J. Cima, *Mater. Des.* **20**, 63 (1999)
62. R. Banerjee, P.C. Collins, D. Bhattacharyya, S. Banerjee, H.L. Fraser, *Acta Mater.* **51**, 3277 (2003)
63. G. Topalov, G. Ganske, E. Lefterova, U. Schnakenberg, E. Slavcheva, *Int. J. Hydrogen Energy* **36**, 15437 (2011)
64. T.L. Zhang, Z.H. Huang, T. Yang, H.J. Kong, J.H. Luan, A.D. Wang, D. Wang, W. Kuo, Y.Z. Wang, C.T. Liu, *Science* **374**(6566), 478 (2021)
65. D.M. Mattox, *Handbook of Physical Vapor Deposition (PVD) Processing: Film Formation, Adhesion, Surface Preparation and Contamination Control* (Noyes Publications, Westwood, 1998)
66. M.A. Herman, H. Sitter, *Molecular Beam Epitaxy: Fundamentals and Current Status*, 2nd., rev. updated edn., Springer Series in Materials Science 7 (Springer, Berlin, 1996)
67. A.E. Danks, S.R. Hall, Z. Schnepp, *Mater. Horiz.* **3**, 91 (2016)

Dong Wang is a professor in the Frontier Institute of Science and Technology at Xi'an Jiaotong University, China. He earned his PhD degree from Xi'an Jiaotong University and subsequently worked as a postdoctoral researcher at The Ohio State University. His research primarily focuses on the microstructure design of functional materials, including shape-memory alloys and ferroelectrics, as well as structural materials such as titanium alloys. He has authored more than 60 papers in high-impact journals. Wang can be reached by email at wang_dong1223@xjtu.edu.cn.

Jiaming Zhu is a professor in School of Civil Engineering at Shandong University, China. He earned his PhD degree in mechanical engineering from The Hong Kong University of Science and Technology and another PhD degree in materials science from Xi'an Jiaotong University. His research interests encompass phase-field modeling, micro-/nanomechanics of solids, shape-memory alloys, phase transitions, and artificial intelligence. He has published more than 40 papers at present. Zhu can be reached by email at zhujiaming@sdu.edu.cn.

Tianlong Zhang is an assistant professor in the Department of Mechanical and Aerospace Engineering at The Hong Kong University of Science and Technology. He earned his BS and PhD degrees from Xi'an Jiaotong University, China, and the City University of Hong Kong, respectively. His research is dedicated to the development of advanced structural/functional materials through the principles of microstructure-based alloy design. His contributions have significantly advanced the understanding, prediction, and design of microstructures in materials processing and deformation. He has published papers in various journals such as *Science* and *Acta Materialia*. Zhang can be reached by email at tianlong@ust.hk.

Yunzhi Wang is a professor in the Department of Materials Science and Engineering at The Ohio State University (OSU). His research interests span the areas of modeling and simulation of microstructure evolution during phase transformation and deformation in structural materials, shape-memory alloys and metallic glasses. He is a Fellow of ASM International and The Minerals, Metals & Materials Society (TMS). His awards include the National Science Foundation CAREER Award, Harrison Faculty Award for Excellence in Engineering Education from OSU, Fraunhofer Bessel Research Award from the Alexander von Humboldt Foundation, and Distinguished Scientist Award, Cyril Stanley Smith Award, and William Hume-Rothery Award from TMS. Wang can be reached by email at wang.363@osu.edu.